Acta Mechanica Sinica (2020) 36(2):320–338
https://doi.org/10.1007/s10409-020-00947-2

RESEARCH PAPER

Unsteady aerodynamic characteristics of a horizontal wind turbine under yaw and dynamic yawing

Zhaoliang Ye[1,2] · Xiaodong Wang[1] · Ziwen Chen[1] · Luyao Wang[1]

Received: 1 September 2019 / Revised: 25 January 2020 / Accepted: 29 February 2020 / Published online: 10 April 2020

Abstract
Horizontal axis wind turbine (HAWT) often works under yaw due to the stochastic variation of wind direction. Yaw also can be used as one of control methods for load reduction and wake redirection of HAWT. Thus, the aerodynamic performance under yaw is very important to the design of HAWT. For further insight into the highly unsteady characteristics aerodynamics of HAWT under yaw, this paper investigates the unsteady variations of the aerodynamic performance of a small wind turbine under static yawed and yawing process with sliding grid method, as well as the there-dimensional effect on the unsteady characteristics, using unsteady Reynolds-averaged Navier–Stokes (URANS) simulations. The simulation results are validated with experimental data and blade element momentum (BEM) results. The comparisons show that the CFD results have better agreement with the experimental data than both BEM results. The wind turbine power decreases according to a cosine law with the increase of yaw angle. The torque under yaw shows lower frequency fluctuations than the non-yawed condition due to velocity component of rotation and the influence of spinner. Dynamic yawing causes larger fluctuate than static yaw, and the reason is analyzed. The aerodynamic fluctuation becomes more prominent in the retreating side than that in the advancing side for dynamic yawing case. Variations of effective angle of attack and aerodynamic forces along the blade span are analyzed. The biggest loading position moves from middle span to outer span with the increase of yaw angle. Three-dimensional stall effect presents load fluctuations at the inner board of blade, and becomes stronger with the increase of yaw angle.

Keywords Wind turbine · Three-dimensional stall effect · Numerical simulation · Dynamic yawing

Abbreviations

BEM	Blade element momentum
CFD	Computational fluid dynamic
SCADA	Supervisory control and data acquisition
FAST	Fatigue aerodynamic structure turbulence software
URANS	Unsteady Reynolds averaged Navier–Stokes equations
T-SST	Transient shear stress turbulence model
HAWT	Horizontal axis wind turbine
D	Wind turbine diameter
$\boldsymbol{\gamma}$	Yaw angle
$\boldsymbol{\varphi}$	Azimuth angle
$\boldsymbol{\beta}$	Pitch angle
AoA	Angle of attack
$\boldsymbol{\alpha}_{\text{geom}}$	Geometric angle of attack
$\boldsymbol{\alpha}_{\text{eff}}$	Effective angle of attack
V_0	Inflow velocity
V_{rel}	Relative velocity
$\boldsymbol{\omega}$	Rotation speed of wind turbine
t	Time
f	Shedding/meandering frequency
S_t	Strouhal number
R_e	Reynolds number
C	Chord length at the spanwise airfoil
$\boldsymbol{\lambda}$	Blade tip speed ratio
C_n	Normal forces coefficient on the local airfoil
C_t	Tangential forces coefficient on the local airfoil
C_l	Lift forces coefficient
C_d	Drag forces coefficient
C_X	Tangent forces coefficient on the rotational plane

✉ Xiaodong Wang
wangxd@ncepu.edu.cn

[1] Key Laboratory of Power Station Energy Transfer Conversion and System, Ministry of Education, North China Electric Power University, Beijing 102206, China

[2] China Huaneng Clean Energy Research Institute, Beijing 102209, China

C_Z	Axial forces coefficient on the rotational plane
C_p	Pressure coefficient
C_{po}	Power coefficient
C_t	Thrust coefficient
T	Wind rotor torque
F_t	Wind rotor thrust

1 Introduction

Wind power has grown rapidly in past decades. The aerodynamics of the wind turbine is the key point of wind power generation. Due to the stochastic property of wind, the wind turbine often works under yaw where the rotor disk is not perpendicular to the wind direction. Under a yawed condition, the upstream wind has a velocity component that is parallel to the rotational plane. Thus, the angle of attack (AoA) of the blade has a periodic variation in one resolution [1]. The aerodynamic performance of the wind turbine under yaw, as well as the surrounding flow, shows highly unsteady characteristics, resulting in high fatigue load and degrading the operational life of wind turbine. Insightful understanding of the unsteady characteristics of the aerodynamic performance and surrounding flow of wind turbine under yaw is of great significance for wind turbine design [2].

The aerodynamics of a wind turbine under yaw has been investigated extensively using both experiments and numerical simulations. The measurements on aerodynamic performance along the blade in combination with the detailed flow field help to understand the flow mechanism. Hand et al. [3] performed wind tunnel experiments on National Renewable Energy Laboratory (NREL) Phase VI, a two-bladed wind turbine, providing a benchmark for numerical simulations. Pressure and aerodynamic force coefficients at different radial locations were obtained under five yawed cases. The AoA was found varying with the blade azimuth angle approximately in a sinusoidal function. Schepers et al. [4] performed wind tunnel experiments on a three-bladed wind turbine, MEXICO rotor under three yawed angles. Sectional aerodynamic force and torque variations with the azimuth angle were obtained. It is found that the sinusoidal variation rule is not correct at the inner span of the blade due to the velocities induced by the root vortices. Sant [5] investigated the TUDelft reference rotor in an open jets wind tunnel under both axial and yawed conditions. In their work, the limitations of blade element moment (BEM) method to the skewed wake under yawed conditions were assessed. Based on the work of Schepers et al. [4], Micallef et al. [6] performed stereo particle image velocimetry measurements to study the blade aerodynamic performance and near wake development. They found that under yaw the flow in windward region exhibited inboard motion due to rapid motion of the tip vortices away from the blade. In field test, Ven et al. [7] applied an in-field measurements to investigate the yawed turbine inflow. Along the blade spanwise, an imbalance in the crossflow fraction is shown between azimuth angles of 90° and 270°. This phenomenon is caused by yawed inflow that leads an inwash and outwash on the blade surface. Dai et al. [8] gave a detailed investigation of yaw effect based on the supervisory control and data acquisition (SCADA) data, presenting the characteristics of power coefficient and rotor torque under yaw. Wang et al. [9] investigated the layout of wind turbine site using the control strategies of wake deviation to optimize the utilization efficiency of the offshore wind farm. The above experiments and wind field tests focus had support the development of the numerical simulation method under yaw.

The numerical methods to evaluate the aerodynamic performance of wind turbine mainly include BEM, vortex theory and computational fluid dynamic (CFD). The most commonly used method is BEM, which is fast and low computational costly. Ryu et al. [10] developed a successive under-relaxation technique based on the classical BEM to compute the specified radial locations of the blade, and found the yaw error causes the periodic change of the angle of attack on different span sections. Yaw has influence not only on the wake flow behind the wind turbine, but on the surface flow of blade and three-dimensional (3D) aerodynamic characteristics of rotor [11]. However, the non-uniform flow between blades is still modeled with a simplified wake model based the Prandtl tip loss factor. Moreover, the use of a dynamic inflow model would introduce a time lag to the inflow and load response, complicating the reduced frequency analysis. Both the tip loss model and dynamic inflow model can be possibly improved by free vortex wake method, which combines the blade aerodynamic and wake flow computational model. Qiu et al. [12] investigated the dynamic variation of aerodynamic loads of the wind turbine blade during yaw process with an improved lift line method that introduces a wake model comprising vortex sheet model and tip vortex model, finding that the yaw rate and dynamic wake have obvious effects the shaft thrust and torque of wind turbine. Micallef et al. [1] performed experimental setup and numerical investigations on the topic of tip vortex generation of horizontal axis wind turbine (HAWT) under yaw, and found that vorticity strength on suction side under non-yawed condition were observed to become more concentrated than yawed condition where the vorticity spreads over a small region at the tip.

More accurate numerical models under yaw are presented on the literature. Several aerodynamic correction models, such as the yaw correction by Pitt and Peter [13, 14], dynamic inflow model by Suzuki [15], tip loss model by Prandtl [16], 3D stall delayed model by Du and Selig [17] and wake correction by Buhl [18], have been proposed and widely used, but classical BEM and free wake vortex method (FWM) are still not sufficiently reliable for predicting the aerodynamic

load distributions on the wind turbine blades, especially for the yawed and stalled rotor conditions. Some investigations were performed to investigate the complicated yaw aerodynamic problem of wind turbine using more accurate CFD simulations, with the visualization of detailed three dimensional flow [19]. Tongchitpakdee et al. [20] investigated aerodynamic characteristics of the NREL Phase VI case at several wind speeds under yaw using the Beddoes-Leishman (BL) model, finding that at low wind speeds (<7 m/s) under low yaw angles the flow remains attached over most region of the rotor. Yu et al. [21] performed time-accurate aerodynamic simulations of the NREL Phase VI wind turbine rotor under yawed flow conditions. They found that periodic fluctuation of blade loads at the retreating side has higher magnitudes than that at the advancing side. However, the 3D unsteady stall effect at the different yaw angles was not studied. Schulz et al. [22] investigated a generic 2.4 MW wind turbine with the yaw angle ranging between − 50° and 50° using the FLOWer CFD solver, revealing load variations along the blade spanwise. Jeong et al. [23] investigated the effects of yaw errors on the aerodynamic and aeroelastic behaviors of NREL 5 MW HAWT blade, and pointed out that the impacts of yaw misalignments adversely influenced the dynamic aeroelastic stability of the blade. Dai et al. [24] performed aeroelastic investigations on the Tjæreborg wind turbine under yaw, finding that the fluid–solid coupling gives higher averaged power and thrust, as well as a violent oscillation amplitude.

We found that the unsteady aerodynamic characteristics of the wind turbine blade under yaw considering full 3D rotational effects are still a questionable topic.

Yaw is a continuous moving process with a constant or variable rotational velocity. Few numerical models can be found for the dynamic process. Qiu et al. [12] developed a free vortex method and investigated the torque of the blade and spiral wake flow under a dynamic yawing process with different constant yaw rates (5°/s and 20°/s) for the NREL Phase VI wind turbine. For large utility-scale wind turbines, these yaw rates seem to be unreasonable owing to the larger moment of inertia of the rotor-nacelle subsystem due to enlargement of the blade radius and tower length. Leble et al. [25] carried out a series of CFD simulations to investigate the performance of the DTU 10-MW wind turbine and modeled the turbine as a structured grid with moving boundaries. Simulations were performed with a yaw rate of 0.3°/s and the yaw angle amplitude of 3°. The results showed that the overall power under the dynamic yawing condition was much larger than that of the static yawed case. Then, Wen et al. [26] developed another free vortex method and investigated the NREL 5-MW yawing dynamic sinuous motion with an averaged yaw rate of 1.2°/s and 2.4°/s for the case of $f = 0.1$ Hz and $f = 0.2$ Hz, respectively. The result shows that the dynamic yaw motion induced the upwind and downwind yawing effect, which considerably influenced the AoA of blade sections. As the blade is yawing upwind, the AoA increases and vice versa. With the assumption of the rigid body, Wang et al. [27] gave a research on the start and stop process of wind turbine yawing with the specification of yaw rate ranging from 0°/s to 0.3°/s. The result showed that a faster start and stop process of yawing would cause much more loads fluctuation.

In summary, the unsteady aerodynamic characteristics of wind turbine blades under yaw considering full 3D rotational effects are still unclear. With the assumption of the rigid body, the main contribution of this paper is the proposal of a new grid model methodology for analyzing the overall performance using URANS simulation, aerodynamic loads, and flow field of wind turbines in several static yawed and dynamic yawing processes. The method can be used to analyze interactions between transient aerodynamic phenomena associated with the wind turbine control system. The main objective of this study was to investigate the effects of yaw on the dynamic output power, rotor thrust, and the blade sectional aerodynamic characteristics caused by continuous changes in the yaw angle. The main novelty of the current work is the 3D stall effect analysis under yaw and the inclusion of the dynamic yawing simulation of wind turbine with the multiple structured domain sliding mesh. In the present paper, unsteady CFD simulations are performed to investigate the unsteady aerodynamic characters of a wind turbine blade during the rotational resolution using full 3D wind turbine model.

The paper is organized as follows. Section 2 describes the geometry model and computational method. In Sect. 3, the simulation results under several yaw angles are compared with experimental data. After the work of validation, the discussions mainly focus on the sectional azimuthal variations of aerodynamic force coefficients, as well as the pressure distribution of the blade. Furthermore, the dynamic analysis of overall performance under yawing is interpreted with the comparison of the aerodynamic performance under yaw. Section 4 summarizes the conclusions drawn in this paper.

2 Numerical model

2.1 Case study

Although large-scale multi MW wind turbines have been widely used in recent years, the NREL Phase VI wind turbine still gained many research attentions since detailed measurement data are available for model validation, which is also used for investigation in this paper. The Phase VI wind turbine is a two-blade wind turbine with the airfoil of S809. The rotor diameter is 10.058 m, and hub height is 12.192 m. The rotational speed is 71.9 rpm. The experiment was performed in NASA Ames wind tunnel, which has

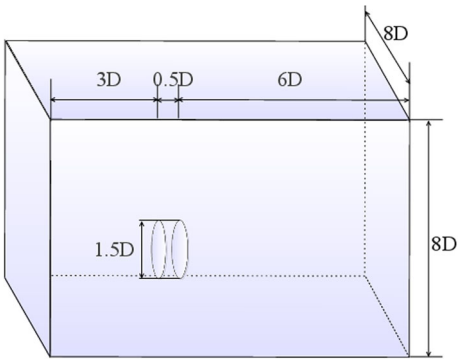

Fig. 1 Computational domain for the simulation of yawed cases

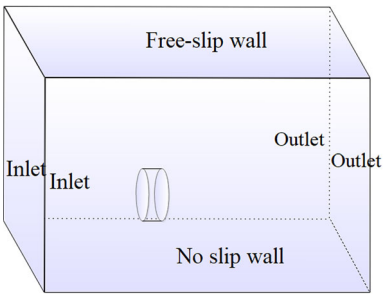

Fig. 2 Boundary conditions used in the simulation

been considered a benchmark for evaluation of the wind turbine aerodynamic model. Detailed geometry parameters and experimental description can be found in NREL report [3].

2.2 Computational domain and boundary conditions

According to the simulation results from Yu et al. [21], the loads are almost the same for rotor-alone model and full wind turbine model. To reduce the computational cost and time, only the wind turbine rotor is modelled in this paper.

The computational domain as shown in Fig. 1 is a rectangle zone with 9.5D in length and 8D in width [24, 28], where D stands for the rotor diameter. The computational domain is divided into two zones: a rotational zone and a stationary zone. The rotor is located at the center of the rotational zone. The rotational zone is a cylinder with the diameter of 1.5D and the height of 0.5D. The distance between the inlet and the rotational cylinder is 3D.

Figure 2 shows the boundary conditions used in the simulations. Uniform wind speed of 7 m/s is set as the inlet of the domain with a turbulence intensity of 5%. The boundary conditions for the top and down plane in the domain are free-slip and no-sip walls. The blade surface is set to no-slip wall. A pressure outlet condition is assigned to the outlet of domain. The inlet velocity direction varies to generate different yaw angles.

2.3 Computational grid

As shown in Fig. 3, a multi-block structured grid is generated in the rotational zone using AutoGrid from NUMECA software. The grid number for this zone is about 4.79 million. The total grid number including stationary zone is about 6.7 million. In order to resolve the boundary layer, the grids around the blades are refined to keep the y^+ less than 5 on the blade surface.

2.4 Numerical methods

Commercial software CFX is used to solve the unsteady URANS. The sliding mesh is used for data exchange between the rotational zone and the stationary zone. For the time-accurate calculations, a dual-time implicit time integration algorithm is used. The time-step size is equivalent to an azimuthal angle increment of 2.5°, coupled with 20 pseudo-time sub-iterations. The residual of the continuity equation is reduced by at least three orders throughout the calculations. For comparison and validation, BEM simulations using FAST software were also performed.

The definition of dynamic yawing with the moment of sinusoidal is depicted below. Following the prior researches [25–27], a sinusoidal pitching motion is specified for the dynamic yawing of NREL Phase VI:

$$\Omega = RPM \sin(\omega t + \varphi_0), \tag{1}$$

where Ω is the wind turbine yaw velocity, $RPM = 5°/s$ (the amplitude). According to the description of extreme wind direction change in the IEC61400-5, the duration is 6 s (which means wind turbine will yaw from 0° to 30° within 6 s). ω is the circular frequency, and it is also denoted as $\omega = 2\pi f$, where f is the yawing frequency (which is equal to 1/24). t is the time. φ_0 is the initial phase. It is assumed that $\varphi_0 = 0$. Variation of the yaw rate is shown in Fig. 4a. Owing to the change of yaw rate, the yaw angle changes with certain law like Fig. 4b. The free-stream velocity V_0 is constant and equals to 11.4 m/s for all simulation cases.

2.5 Extracting sectional physical variables

Figure 5 illustrates the definition of the yaw angle and azimuth angle of wind turbine rotor. The yaw angle is defined as the angle between inflow and the rotational axis. The wind turbine rotates counter-clockwise, defining Blade 2 at top position with azimuth angle $\varphi = 0°$.

In order to evaluate the sectional variations of the aerodynamic loads, the blade will be divided into a number of spanwise sections. At each section, the pressure is integrated along the chord-wise direction and resolved in the global coordinate system to produce the spanwise variation of the

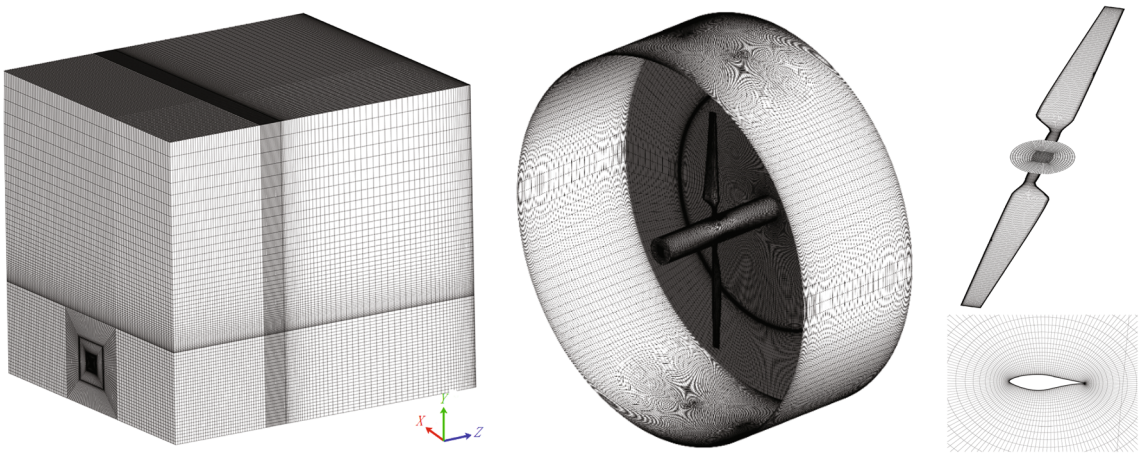

Fig. 3 Far field mesh and blade region mesh in the rotational zone

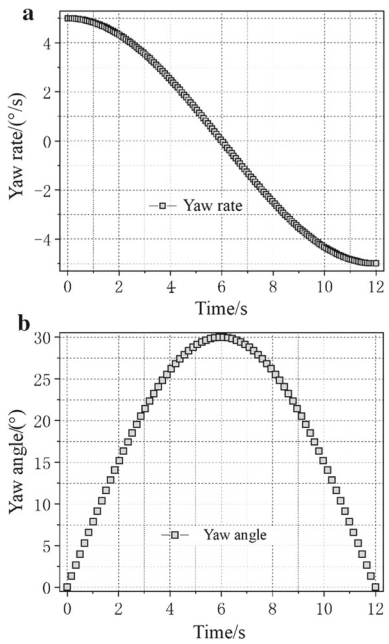

Fig. 4 Illustration of the yawing process: **a** variation of yaw rate, **b** variation of yaw angle

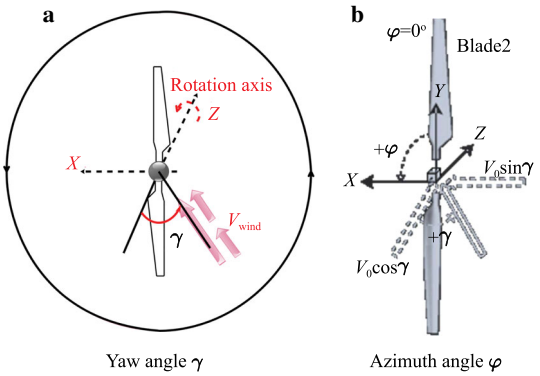

Fig. 5 **a** Yaw angle γ of wind turbine rotor and **b** azimuth angle φ of blade

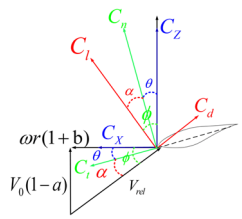

Fig. 6 Definition of aerodynamic force coefficients

normal and tangential forces coefficient (C_n and C_t), as shown in Fig. 6. Here, the axial force coefficient refers to the force component parallel with the global Z axis, and the tangential force coefficient, refers to the force component parallel to the global X axis.

If the yaw angle is zero, the syntactic velocity keeps the same during revolution, which can be calculated as follows,

$$V_{rel} = \sqrt{(V_0)^2 + (\omega r)^2}. \tag{2}$$

When the yaw angle is not zero, the syntactic velocity needs to be updated with the change of azimuth angle. For yawed cases on one revolution, as shown in Fig. 7, the azimuth angle is defined as the angle from the red solid arrow line to the black solid arrow line. At zero azimuth angle, the blade is retreating the tangent component of inflow velocity, leading to a lower synthetic velocity and a higher angle of attack. On the other hand, with the azimuth angle of 180°, the blade is advancing toward the velocity component aligned tangent to the rotor plane, leading to a higher syntactic velocity and a lower angle of attack. Neglecting the torsional deformation along the blade spanwise, the trend of angle of attack relative to the azimuth angle should be identical to the inflow angle. Consequently, for the current case, the angle of attack reaches the maximum and minimum at azimuth angles

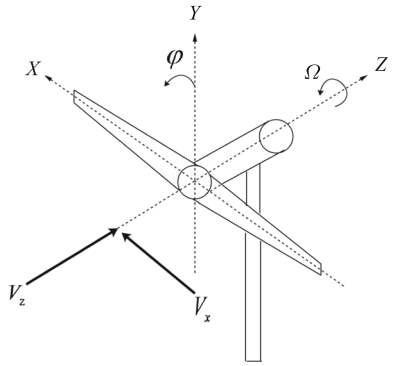

Fig. 7 Aerodynamic analysis on one revolution

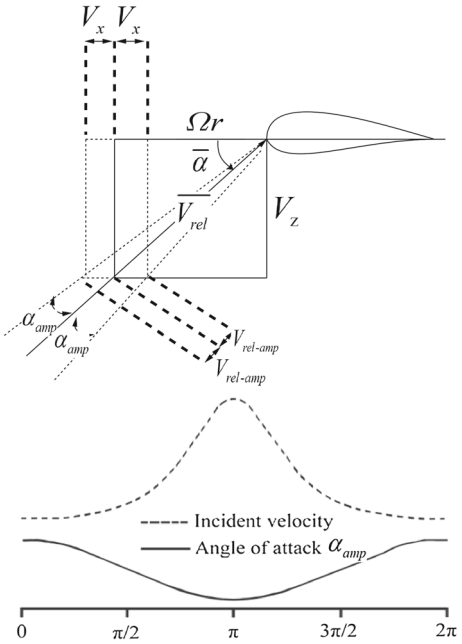

Fig. 8 Definition of AoA α

of 0° and 180°, respectively. The syntactic velocity and the angle of attack at different spans will change continually in one revolution. The AoA α is defined in Fig. 8, $\overline{\alpha}$,α_{amp},$\overline{V_{rel}}$, $V_{rel-amp}$ are the averaged AoA, azimuthal AoA, mean syntactic velocity, and azimuthal syntactic velocity, respectively. The syntactic velocity V_{rel} can be calculated as follows

$$\alpha_{\text{geom}} = \arctan\left[\frac{\cos\beta\cos\gamma - \sin\beta(\lambda - \sin\gamma\cos\varphi)}{\cos\beta(\lambda - \sin\gamma\cos\varphi) + \cos\gamma\sin\beta}\right], \tag{3}$$

$$V_{rel} = \sqrt{(V_0\cos\gamma)^2 + (\omega r - V_0\sin\gamma\cos\varphi)^2}, \tag{4}$$

where β, γ, φ stand for the pitch angle, yaw angle, azimuth angle, respectively.

When the azimuth angle is between 90° and 270° (advancing side), the absolute velocity become bigger than that when the azimuth angle is between − 90° and 90° (retreating side).

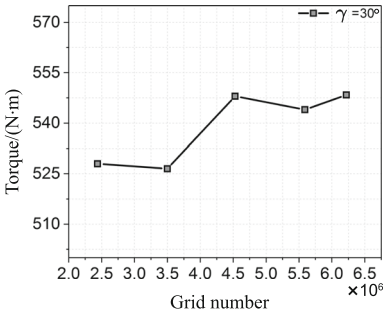

Fig. 9 Torque calculated with different numbers of grid

On the advancing side, the wind velocity component aligned tangent to the rotor plane is opposite to the linear velocity, so that the synthetic velocity becomes higher. On the retreating side, the wind velocity component is in the same direction to the linear velocity, thus the synthetic velocity becomes smaller.

3 Results and discussions

Nine simulation conditions with yaw angle of 0°, 5°, 10°, 15°, 20°, 25°, 30°, 45° and 60° are investigated. The dynamic yawing with the law of sinusoidal is also carried out in the paper. The total aerodynamic performance and frequency characteristics are discussed first for results validation. In what follows, the aerodynamic characters and 3D stall characters at different span sections are discussed.

3.1 Verification and validation

3.1.1 Grid independence

Figure 9 shows the calculated torque of wind turbine at yaw angle of 30° using different numbers of grid (2.24–6.22 million for the rotor mesh). Unsteady computations were performed to study the grid independence. It is seen that the difference between calculated torques is very small when the grid number is over 4 million. Thus, the middle size grid (4.53 million) is selected at the end.

3.1.2 Turbulent model independence

Three turbulence models, $k-\omega$ model, shear stress transport (SST) model, and transitional SST (T-SST) model, are analyzed to check the model dependence. Table 1 shows the calculated torque of wind turbine rotor at $\gamma = 30°$. It is seen that in the $k-\omega$ model and SST model the aerodynamic losses of wind turbine were over predicted due to the full turbulence assumption. The T-SST model gave much better prediction

Table 1 Rotor torque (N·m) calculated using different turbulence models

Exp	Turbulent models		
	$k-\omega$	SST	T-SST
571.42	485.58	480.65	548.01

Table 2 Rotor torque (N·m) calculated using different time step size

Exp	Time step		
	72	144	360
571.4	548.01	524.87	540.6

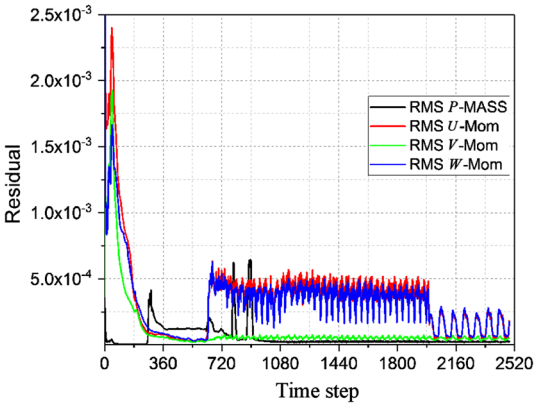

Fig. 10 Residual convergence curve at $\gamma = 30°$

with the relative error of about 4%. So the T-SST model is chosen for our study.

3.1.3 Verification for the unsteady time steps

In the unsteady computations, the time step size may have influence on the calculated aerodynamic performance. Three different time step sizes with step number of 72, 144, and 360 in one revolution were studied. Table 2 shows that calculated rotor torque under 30° yaw angle. It illustrates that the time step size has a small influence on the torque. The difference between results is less than 4%. Considering the computational cost and accuracy, time step of 72 is selected for following studies.

3.2 Averaged results

The convergence history of mean square residual for mass and momentum equations at $\gamma = 30°$ are shown in Fig. 10. The unsteady computation started based on 600 steady iterations. The convergence errors are below 10^{-4}. The residual curves for other yaw cases are similar to the curves in this figure. Figure 11 show the thrust convergence distribution under different yaw angles. After about 20 revolutions computation, the curves show periodic oscillations and keep stable. The computations are considered as converged.

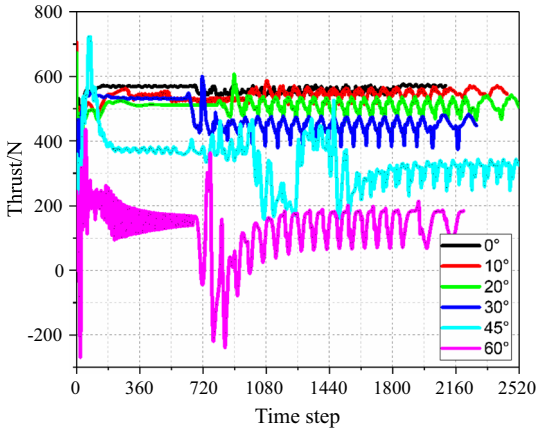

Fig. 11 Thrust convergence curve under yaw

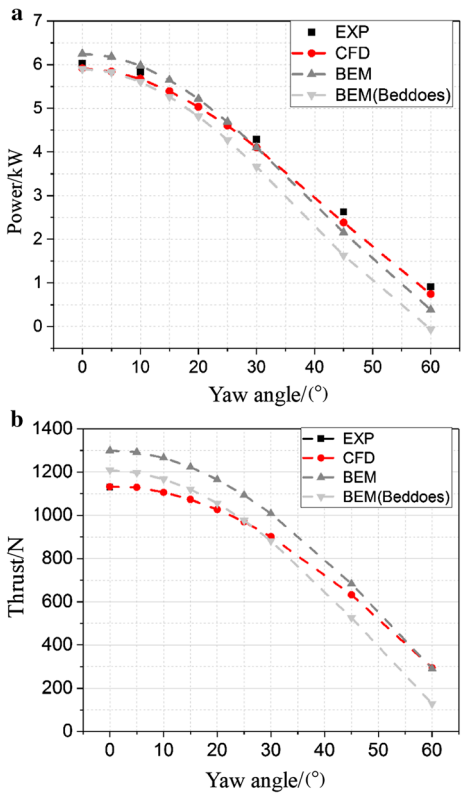

Fig. 12 **a** Power and **b** thrust generated for wind turbine rotor running at different yaw angles

Figure 12a shows the calculated wind turbine power for nine yaw conditions. The experimental data, the BEM results with and without Beddoes stall model are also presented. It is seen from the comparison that the CFD results give better agreement with experimental data than BEM results, especially for largely yawed conditions. The Beddoes model improves the BEM results under small yaw angles. However, it over amended the BEM results under large yaw angles.

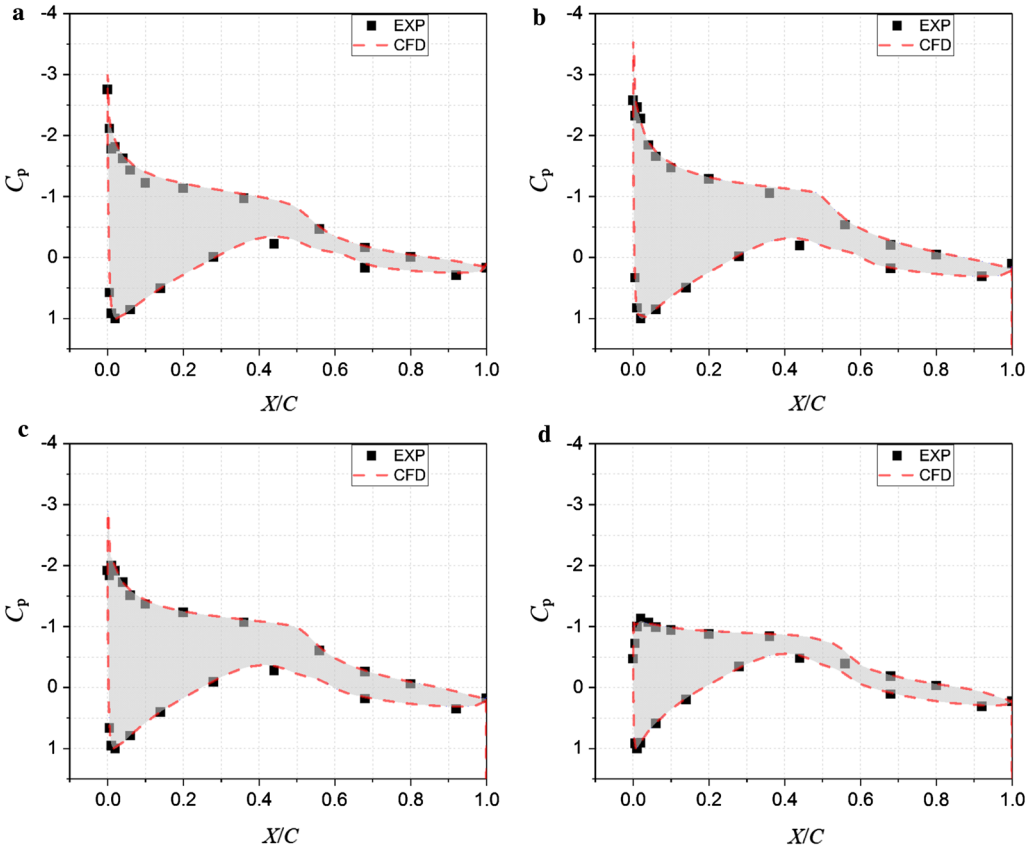

Fig. 13 Pressure coefficient distributions at four spanwise sections under non-yawed condition: **a** $r/R = 0.3$, **b** $r/R = 0.47$, **c** $r/R = 0.63$, **d** $r/R = 0.95$

Comparing with the result for non-yawed condition, the averaged powers under yaw angles of 10°, 30° and 60° decrease by 4.265%, 29.9% and 86.8%, respectively. Under yawed conditions, the velocity component of the incoming flow normal to the rotor plane decreases by cos γ. While, the power varies approximately in $\cos^2\gamma \sim \cos^3\gamma$ due to the combined effect of wind component normal to the rotor plane and wind component aligned tangent to rotor plane.

The variations of axial thrust for different yaw angles are shown in Fig. 12b. Compared with the result of non-yawed condition, the thrust decrease by 2.32%, 20.37% and 73.98% under yaw angles of 10°, 30° and 60°, respectively, which decreases in cos γ function. For the thrust, the experimental data only for non-yawed condition is available. The BEM method over predicates the thrust by about 18%. Same to the power curves, the Beddoes model improves the BEM performance under small yaw angles. However, it over-amends the BEM results obviously under large yaw angles comparing to CFD results.

Figures 13 and 14 show the distributions of pressure coefficient on blade surface at four different span sections under $\gamma = 0°$ and $\gamma = 30°$. In these figures, the pressure is averaged over one rotor revolution. In general, the comparison shows that CFD results have good agreement with the experiment data. When wind turbine operates in yawed conditions, the wind velocity component vertical to the rotational surface decreases, reducing the airfoil aerodynamic performance, which can be seen from the decreasing of the maximum C_p, especially at inner and middle span sections.

In Figs. 15 and 16, the radial distribution of the azimuthal-averaged normal force coefficient (C_n) and tangential force coefficient (C_t) are presented for four yaw angles. The error bar shows the standard deviation of measurement. It is seen that the computational results have good agreements with experimental data in general, excepting that for $\gamma = 60°$. The standard deviation of measurement at the blade root is larger than that at the blade tip, due to the strong flow separation and the 3D effect of the centrifugal and Coriolis force at the root. The CFD result exceeds the measurement error bar at outer span when yaw angle reaches 60°, which means RANS simulations have not predicted aerodynamic forces well at the high yaw angle. For small yaw angles, the maximum C_n locates at around 40% span. With the increase of yaw angle, C_n decreases and the location of maximum C_n moves to outer span. The curve of C_n is getting flat. With the increase

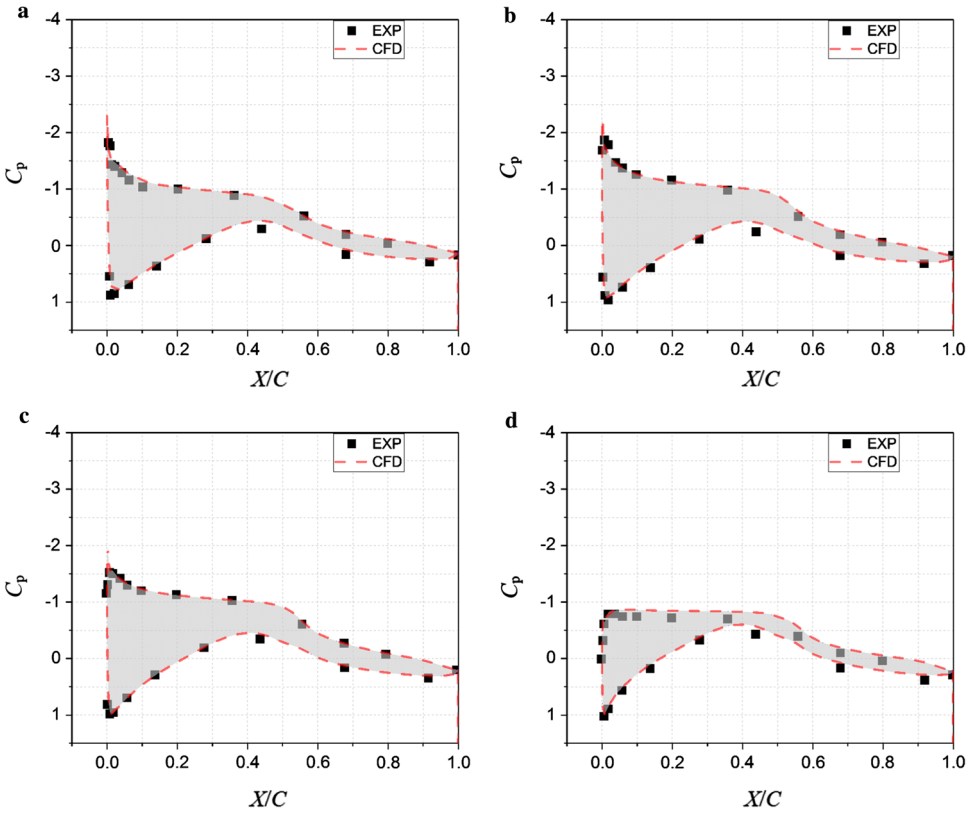

Fig. 14 Pressure coefficient distributions at four spanwise sections under $\gamma = 30°$: **a** $r/R = 0.3$, **b** $r/R = 0.47$, **c** $r/R = 0.63$, **d** $r/R = 0.95$

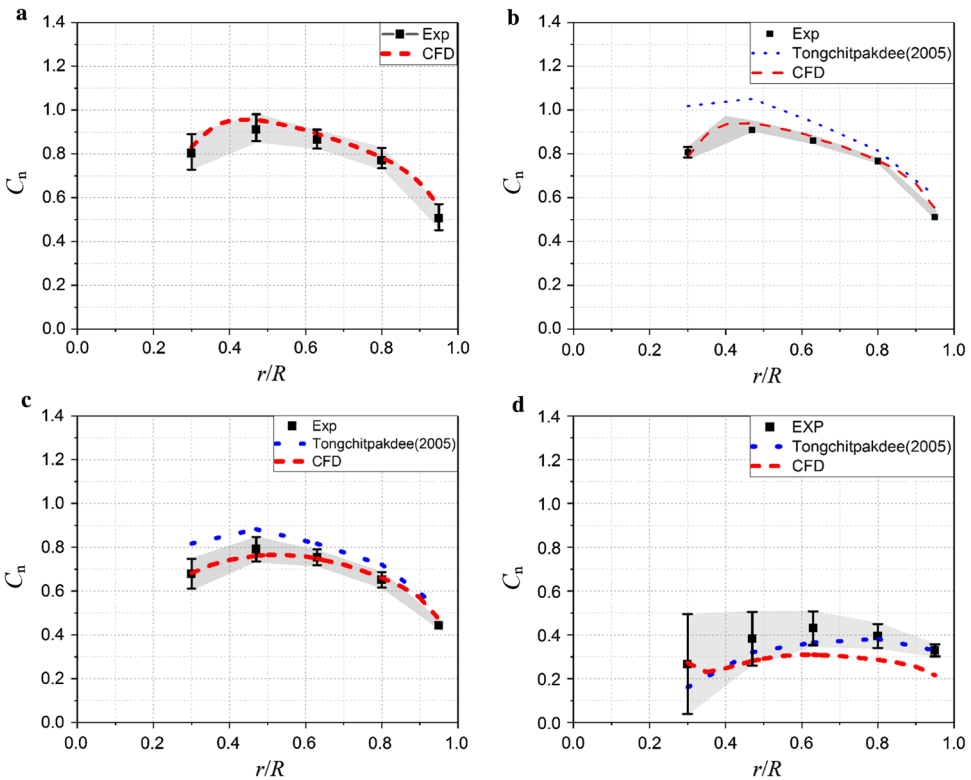

Fig. 15 Comparison of C_n at different span sections under different yaw angles: **a** $\gamma = 0°$, **b** $\gamma = 10°$, **c** $\gamma = 30°$, **d** $\gamma = 60°$

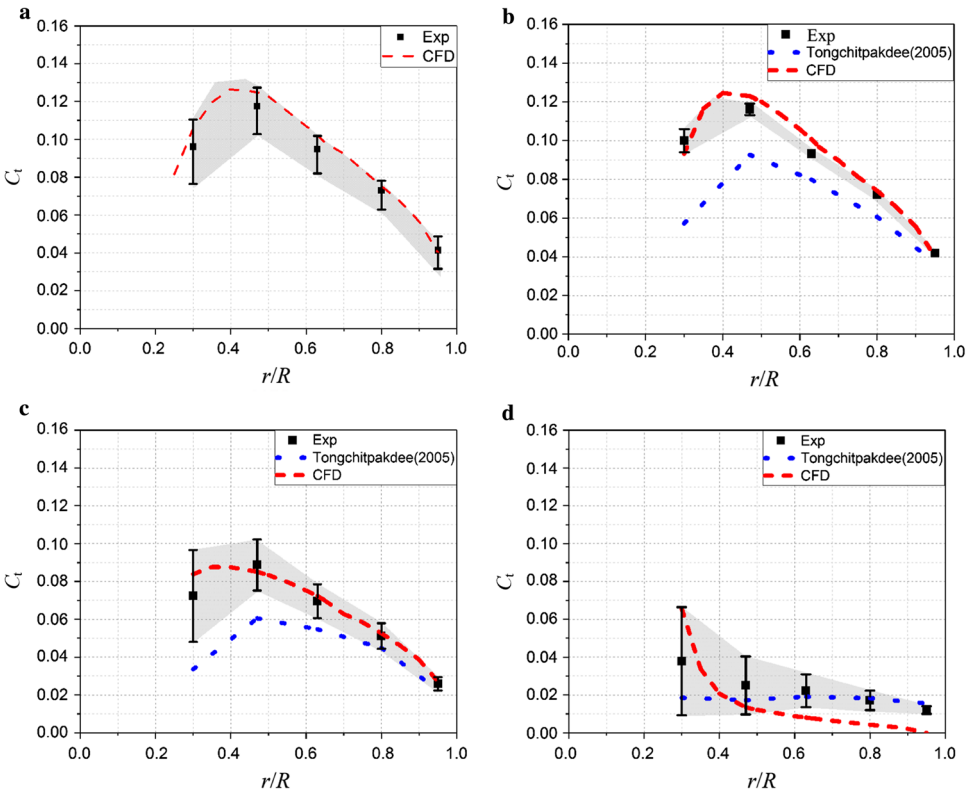

Fig. 16 Comparison of C_t at different span sections under different yaw angles: **a** $\gamma = 0°$, **b** $\gamma = 10°$, **c** $\gamma = 30°$, **d** $\gamma = 60°$

of yaw angle, C_t also decreases and the location of maximum C_t moves to inner span.

3.3 Time dependent analysis

The results of twelve rotor revolutions are analyzed. In each revolution, 72 samples of torque are collected. Fast Fourier transformation is applied to get the rotor aerodynamic frequency. Figure 16 shows the torque spectra of single blade under different yaw angles. The blade passing frequency is 1.198 Hz (base frequency). When the yaw angle is zero, the fluctuation is negligible. The possible reason for the fluctuation is the excitation of crossflow and inflow direction, which has been mentioned by Vey et al. [7] and Shirakashi et al. [29]. The main frequency is about 4.7878 Hz, four times of blade passing frequency. Under lightly yawed conditions, a fluctuation with the passing frequency is observed. The reason for this fluctuation is that the rotational velocity has a component parallel to the incoming velocity. The direction of this component is positive in advancing process and negative in retreating process, leading to the relative velocity and output power decreasing in advancing process and increasing in retreating process, as can be seen from Fig. 17. With the increase of the yaw angle, the fluctuated amplitude is getting larger, and more harmonics with higher frequency are observed, which are mainly caused by the variation of the rotational velocity component. To investigate the root vorticity effects further, the blade is divided into nine spanwise segments with equal length. Figure 18 shows the torque variation respecting to the azimuthal angle at each span section. The sum of torque at all segments equal to the total torque of the whole blade. For non-yawed case, it is seen that the torque components at middle and outer span keep constant. While, small fluctuations of torque component can be observed at inner span, $<30\%$ for the current case, which is identified in the frequency spectrum Fig. 16. Actually the variation of torque is direct related to the velocity. Wang et al. [30] found that nacelle wind speed is mainly influenced by the dynamic inflow, which is similar to the current analysis. It is also seen that the major contribution of torque output is from middle span segments, i.e., sections of 8, 7, 6, 5 in this case. The inboard torque distribution presents more fluctuations under yaw, especially at high yaw angles. For instance, as shown in Fig. 17 $\gamma = 10°$, obvious fluctuations of torque can be seen at middle and outer span sections. The frequency equals to the blade passing frequency. For higher yaw angle, sharp drops of torque are observed at inner sections of 2, 3, 4, which is the influence of spinner. Figure 19 presents the spectrum of rotor torque using FAST computation results. Only the two periodic (2p) pulse is observed for all conditions. The

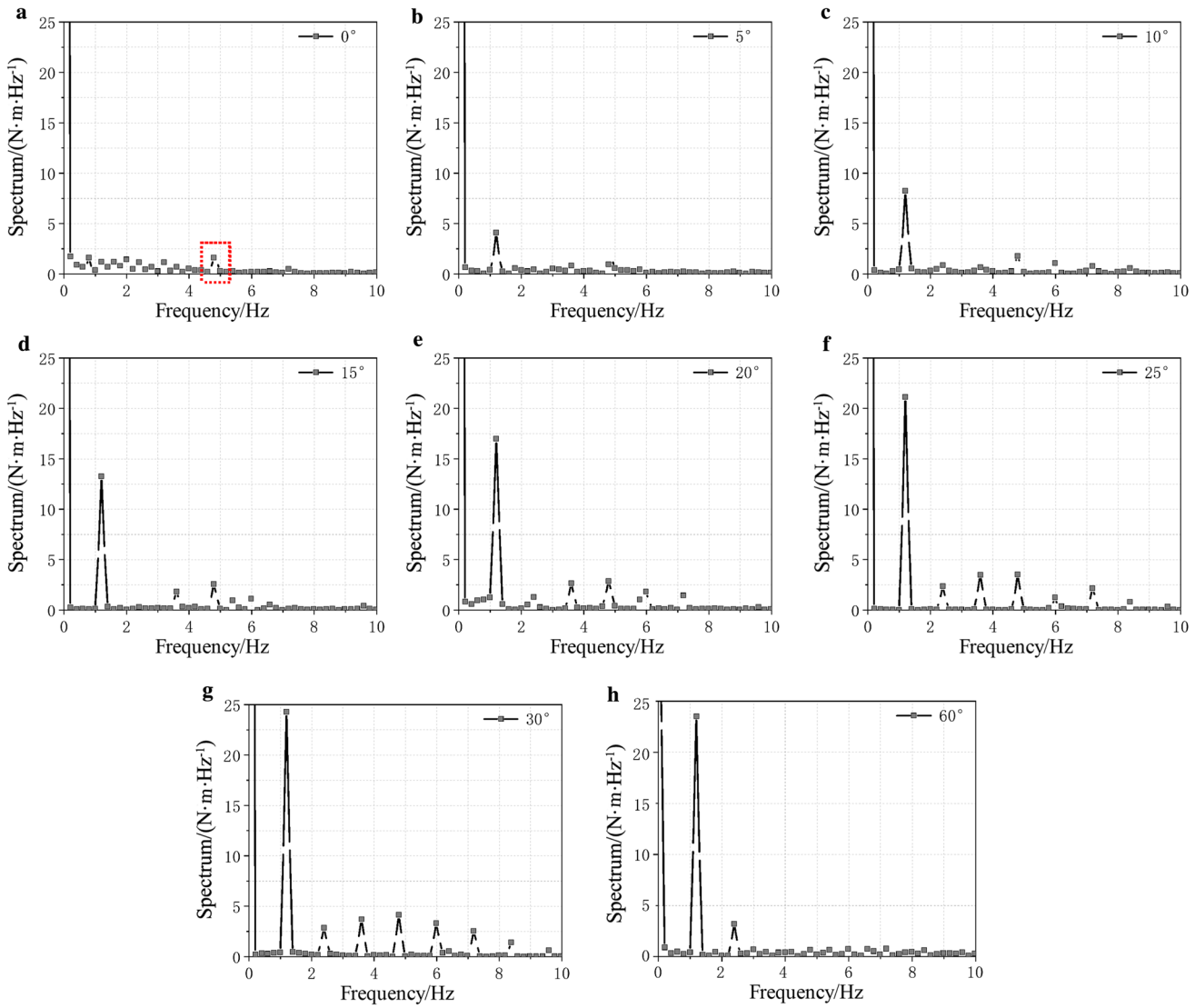

Fig. 17 Frequency of single blade torque under different yaw angles

fluctuations due to 3D vortices and spinner effect cannot be captured.

The azimuthal variations of AoA at four span sections are shown in Fig. 20. At the non-yawed condition, the AoA keep constant during revolution. For yawed cases, the AoA decreases among the process of azimuth angle from 0° to 180° (downstroke) and increases among the process of azimuth angle from 180° to 360° (upstroke). With the increase of yaw angle, the variation of AoA becomes larger. And the variations of AoA at inner span and middle span are much larger than that at outer span, which means the decrease of aerodynamic performance is more severe at the middle and inner span.

Figure 21 shows normal force coefficient distribution at the radial position, $r/R = 0.3$ varying with the azimuth angle under nine different yaw angles. Three simulation results of CFD, FAST computations with and without Beddoes model are presented. The aerodynamic force coefficient curves are similar in general. CFD result shows a higher magnitude of the C_{n} at the zero azimuth angle than that of other two results. Due to the influence of spinner, there is a large drop of C_n at around the azimuth angle of 90°. The azimuth angle of the minimum blade loading becomes larger with the increase of the yaw angle.

The azimuthal variations of aerodynamic force coefficient for one blade under yaw angle of 0°, 10° and 30° are shown in Figs. 22 and 23 respectively. For the non-yawed condition, the AoA and other variables almost keep the same in one revolution.

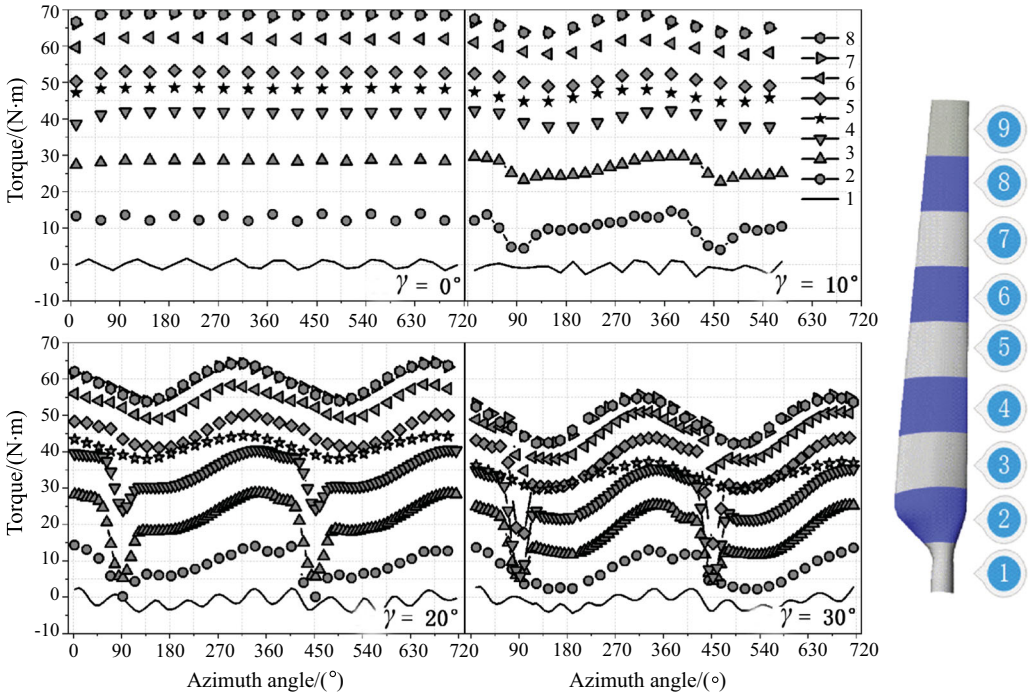

Fig. 18 Torque components along spanwise varying with azimuth angles

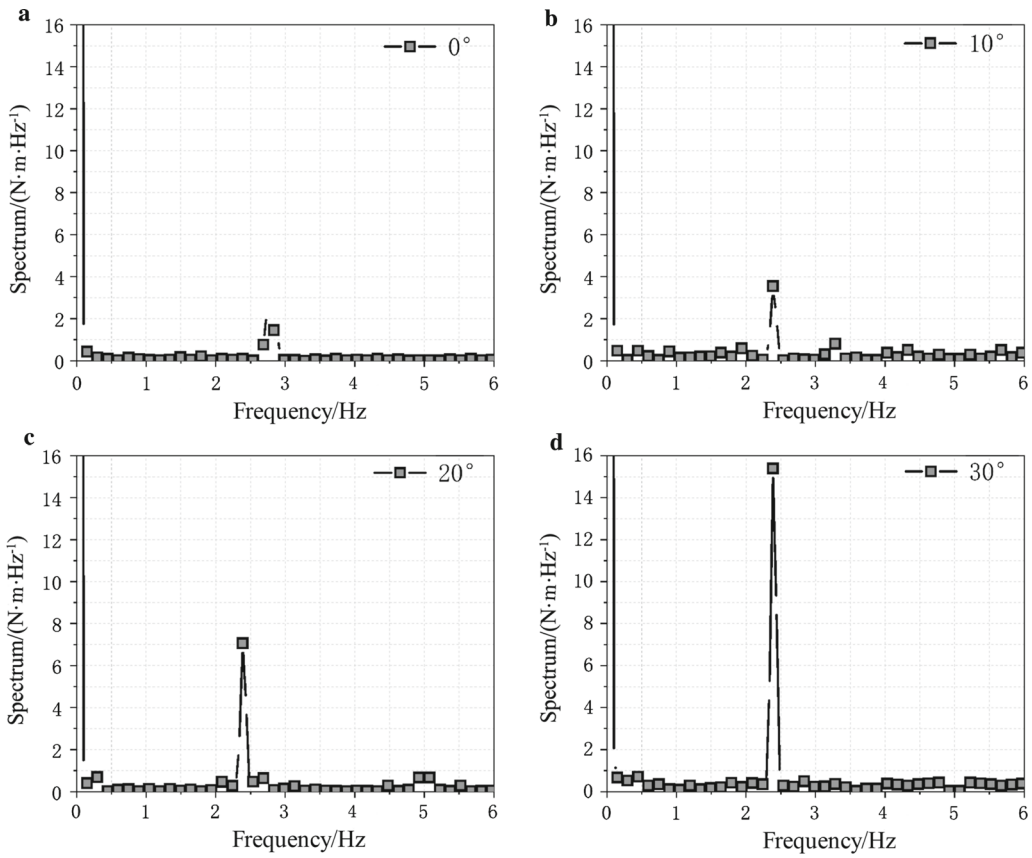

Fig. 19 Frequency response of rotor torque distribution under different yaw angles by FAST without Beddoes

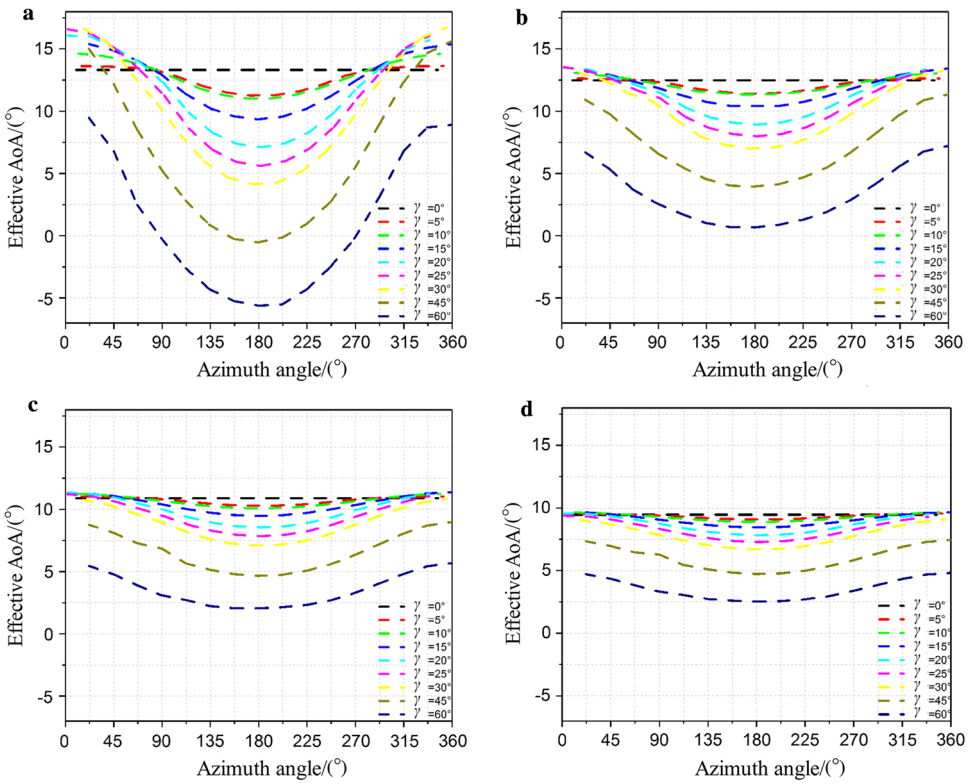

Fig. 20 AOA variations in one revolution under yaw: **a** $r/R = 0.3$, **b** $r/R = 0.47$, **c** $r/R = 0.63$, **d** $r/R = 0.8$

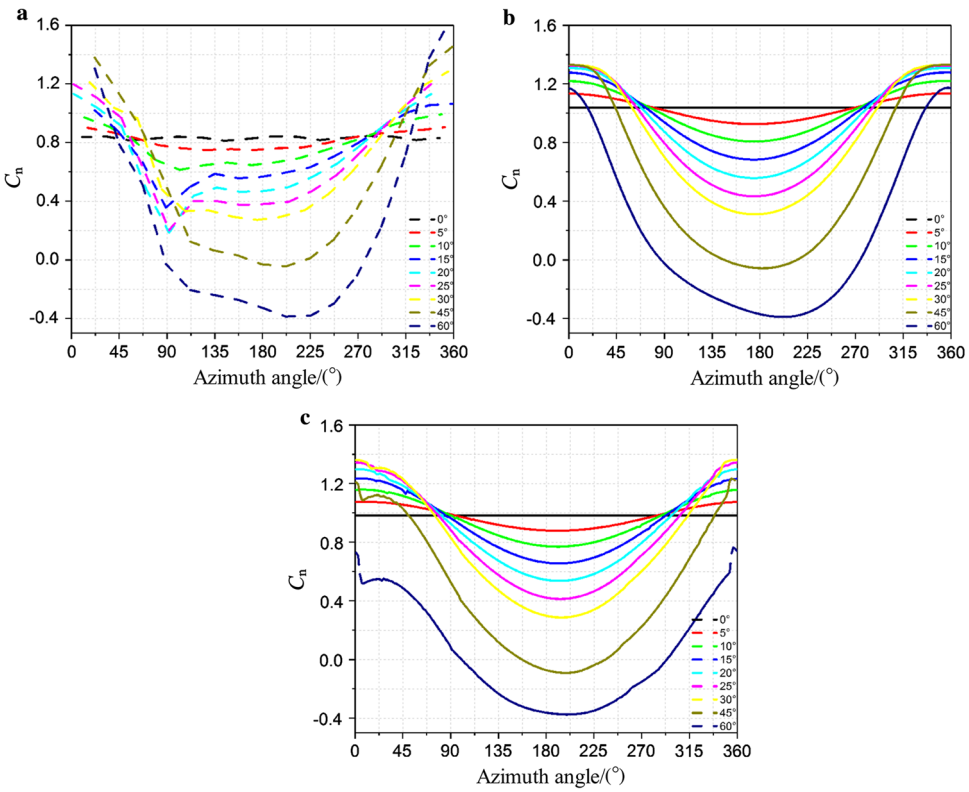

Fig. 21 Normal force coefficient distribution in one revolution under yaw by three computed models ($r/R = 0.3$): **a** CFD, **b** FAST (without Beddoes), **c** FAST (with Beddoes)

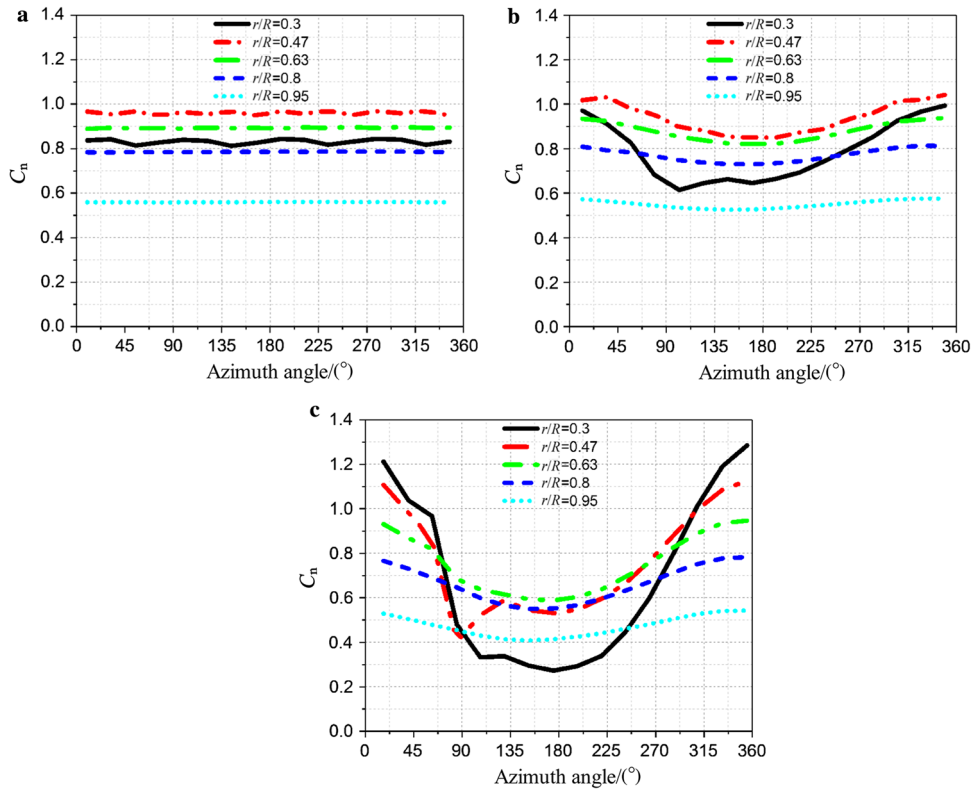

Fig. 22 Normal force coefficient variations in one revolution under yaw: **a** $\gamma = 0°$, **b** $\gamma = 10°$, **c** $\gamma = 30°$

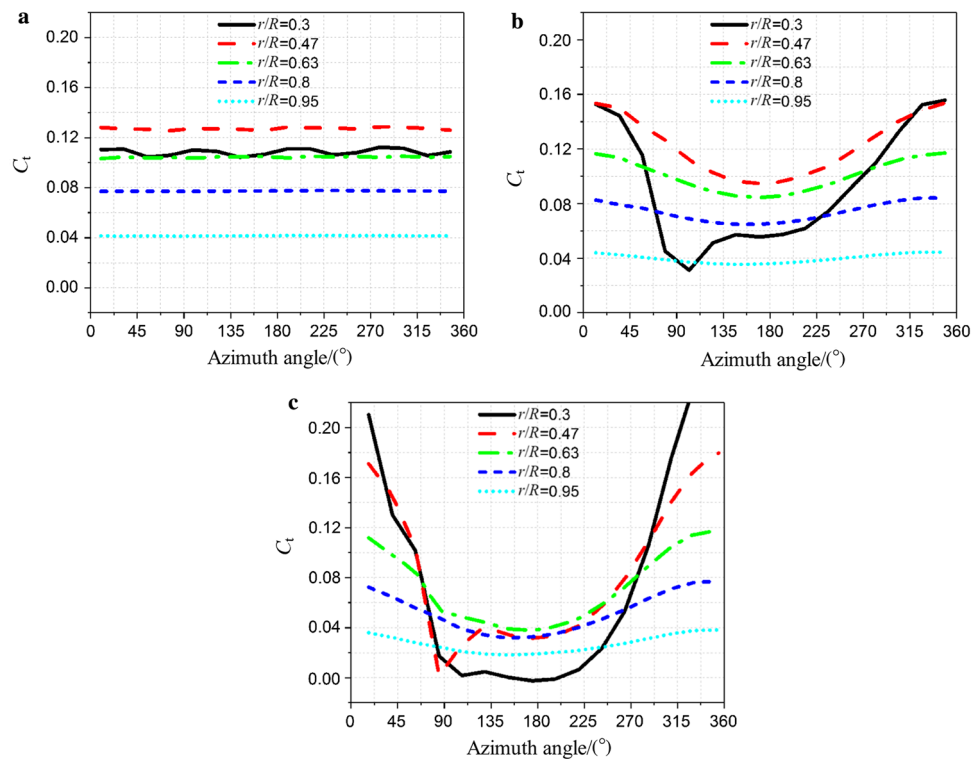

Fig. 23 Tangent force coefficient variations in one revolution under yaw: **a** $\gamma = 0°$, **b** $\gamma = 10°$, **c** $\gamma = 30°$

At the zero azimuth angle, the blade is in retreating process, leading to a higher magnitude of relative velocity and a lower angle of angle attack. On the other hand, at the 180° azimuth angle, the blade is in advancing process, leading to a lower magnitude of relative velocity and a higher angle of attack, shown in Fig. 20. Neglecting the change of pitch angle due to torsional deformation, the trend of angle of attack relative to azimuth angle should be identical as the inflow angle. Consequently, the angle of attack usually reaches the maximum and minimum at azimuth angles of 0° and 180°, respectively. Both the tangential and normal force coefficients variation function with the azimuth angle are the same with the local angle of attack.

The variation of aerodynamic performance at different sections along the blade is different due to the yaw effect. The variations of C_n in one revolution at outer spans, i.e. 80% and 95% spanwise sections, are negligible. C_n at 47% span is largest, while the C_n at 95% span is smallest. At other three spans, C_n curves show slight fluctuations. With the increase of yaw angle, the variations of C_n at inner spans increase. Comparing to non-yawed condition, the C_n increases when the azimuth angle is between 180° and 360°; it decreases when the azimuth angle is between 0° and 180°. Theoretically, the minimum C_n is at the azimuth angle of 180°. The C_n curves at outer span sections agree well with theoretically analysis. As discussed before, there is a large drop of C_n at around the azimuth angle of 90° for 30% and 47% span sections since the blade is just at downstream of the spinner. Also at the inner side of the blade, more separated flow occurs and cosine distribution of aerodynamic force coefficients become more obvious with the increasing of the yaw angle. The variations of C_t shown in Fig. 23 are similar to that of C_n. The two figures show that aerodynamic load variation occurs at inner span of the blade under yaw, which has significant influence on the blade fatigue life. The largest load happened at 0° azimuth angle.

However, the azimuthal variation of aerodynamic force efficiency is a combined effect of change of relative velocity magnitude and orientation of velocity component tangential to rotor plane, even the three dimensional stall effect in the rotation periodic etc. However, the azimuthal variations of tangential and normal force efficiency can be different. Sant [5] carried out the numerical simulation on Mexico wind turbine, and a different azimuthal variation of aerodynamic loads was presented. Lower magnitudes of normal and tangent force coefficient were observed by Sant [5] in region where the blade is retreating toward the wind velocity component aligned tangent to the rotor disk plane (which are higher in current simulation).

The normal force coefficient varying along the blade spanwise are mainly due to the effect of yaw, which leads to the variation of the angle of attack with the azimuth angle at the local airfoil section. Figure 24 shows the radial transient distributions of C_n under nine yaw angles. With the increase of yaw angle, C_n decreases at each span section. The variation of C_n at blade root is larger than that at blade tip. Under small yaw angles (0°, 5°, 10°), the maximum C_n is located at about 40% span section. With the yaw angle increasing, the maximum C_n moves from mid span to outer span. For azimuth angles from − 45° to 45°, C_n decreases almost linearly from inner span to outer span since the radial component effect of inflow is rather small. While, for azimuth angles from 45° to 315°, C_n increases first and then decreases gradually from inner span to outer span. When yaw angle is 30°, the maximum C_n moves to about $r/R = 0.6$, and at higher yaw angles, the maximum load keep stable at the $r/R = 0.7$. At low wind speed, the flow remains mostly attached to the blade surface, except that the small separation at the blade root. The radial flow is also not pronounced.

3.3.1 3D stall effect

Under yawed conditions, 3D rotational stall effect is getting severe, including the dynamic stall and radial flow caused by rotation. Figure 25 shows the normal force coefficient distribution respecting the angle of attack during revolution at yaw angles of 0°, 10°, 25°. The abscissa is the AoA. The red dashed arrow line shows the revolution process with the azimuth angle from 0° to 360°. Label 1 indicates the 0° azimuth angle, i.e. the starting point of the revolution. For comparison, the experiment data from two-dimensional (2D) measurement performed by Somers [31] of Delft University is also presented. The Reynolds number for the experimental data is around 1.0×10^6. The variation range of Reynolds number along the spanwise is between 0.6×10^6 and 1.3×10^6. Figure 28a shows that at the non-yawed condition all C_n have almost no variations during revolutions, except that at the span of 0.3, since the angle of attack does not change. The slight rotational stall effect is observed at the span of 0.3. Comparison with the experimental data, the aerodynamic performance at outer and inner span sections have considerable decrease due to the three dimensional vortices at tip and root. The value of C_n at middle span has good agreement with the experimental data. The 3D effect become more prominent with the increase of the yaw angle. Hysteresis loop occurs firstly at inner span. In the downstroke process, C_n decreases due to the decreasing of AoA; in upstroke process, C_n increases due to the increasing of AoA. The value of C_n in upstroke process is obvious lower than that in the downstroke process at the same AoA. The reason is that the flow on suction surface remains attached during the upstroke process. While, during the downstroke process, the flow starts to separate from the suction surface, and the scale of shedding vortex increases continually with the increase of azimuth angle, till

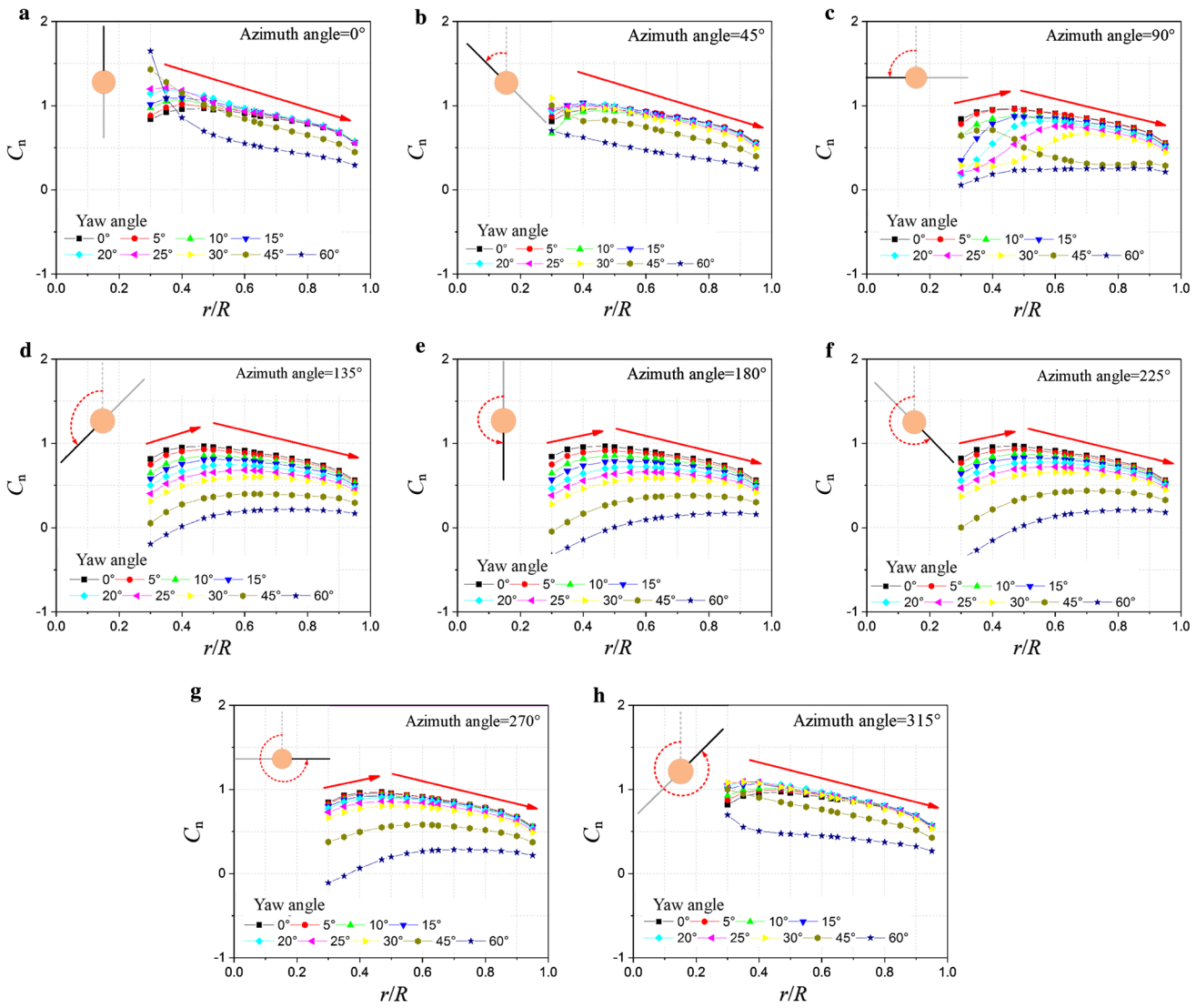

Fig. 24 C_n variation along the spanwise of blade under different yawed conditions at different azimuth angles

about the azimuth angle of 65°–70°. After that, the scale of shedding vortex decreases during the second half downstroke process, and the flow recovers to attachment. When the yaw angle is large, C_n at inner span may exceed the 2D measurement value under high AoA due to the combination effect of dynamic stall and 3D rotational effect.

Figure 26 shows the dynamic variation of C_n on other sections during revolutions. With the increase of yaw angle, the variations of aerodynamic coefficients become much larger. The range of the loop extends to low AoA. When flow is at the 10° fixed yaw angle, the minimal AoA in one revolution is about 11°. Up to the fixed yaw angle of 25°, the minimal AoA in one revolution decreases to about 5°. The wind turbine operates in a long range of low AoA, which decreases the power extraction efficiency of wind turbine largely.

3.4 Comparison of power variation between yawed and yawing simulation

Figure 27 shows the variation of power coefficient between yawed and yawing conditions. The period of the rotation is 0.8344 s. The yawing computational contains aerodynamic performance result of 14 revolutions with the total physics time of 12 s. The result of yawed condition is noted by solid black dot with error bar, while the grey with blade edge dot is identified as the result of yawing case.

With the increase of the yaw angle, the power will decrease, and the fluctuation of the power or torque becomes larger. The additional yaw velocity caused by the dynamic yawing will raise the magnitude of flow velocity vertical to the rotor rotational plane, resulting in a higher value of the power coefficients.

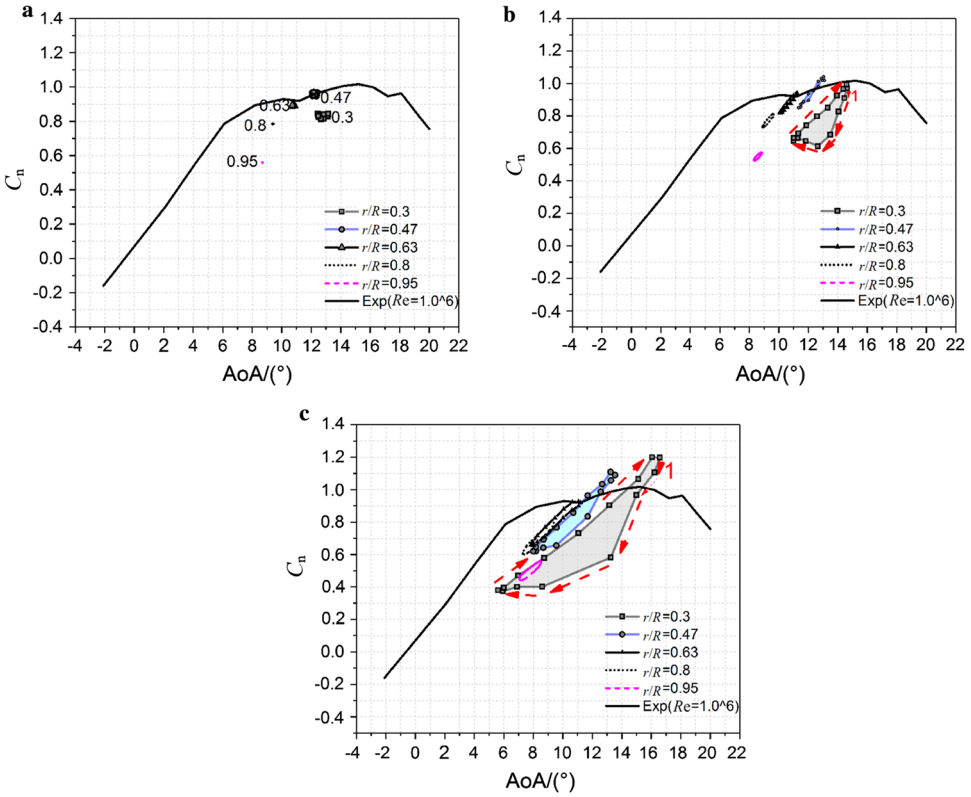

Fig. 25 Hysteresis loop of C_n at three fixed yaw angles: **a** 0°, **b** 10°, **c** 25°

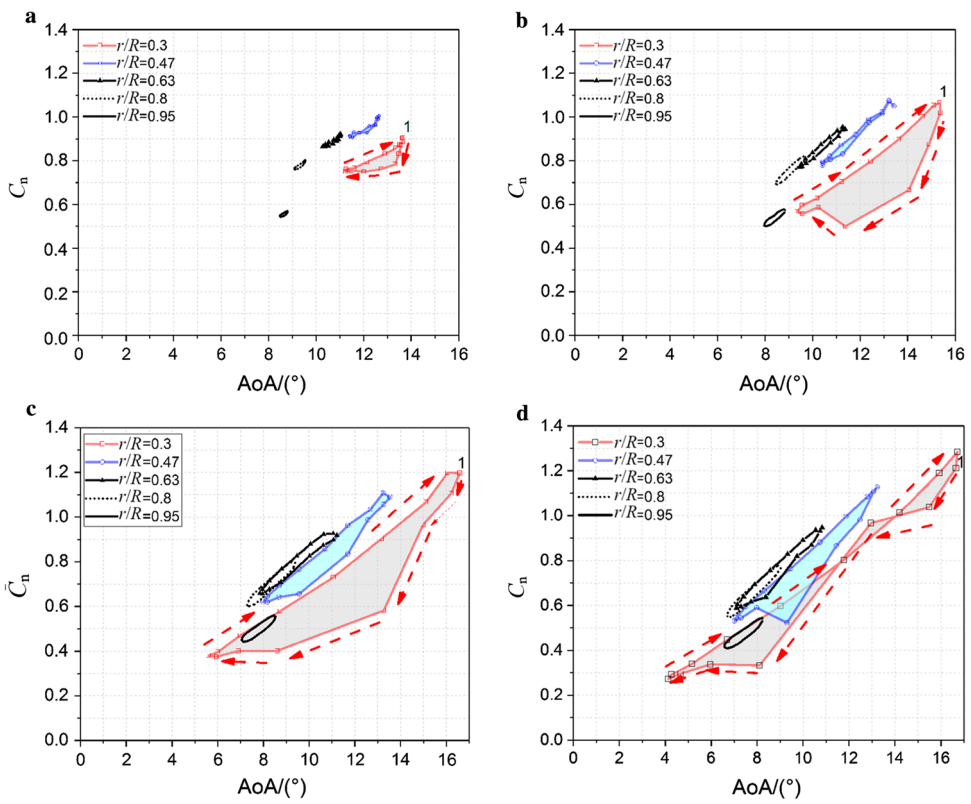

Fig. 26 Hysteresis loop of C_n at different yaw angles: **a** 5°, **b** 15°, **c** 25°, **d** 30°

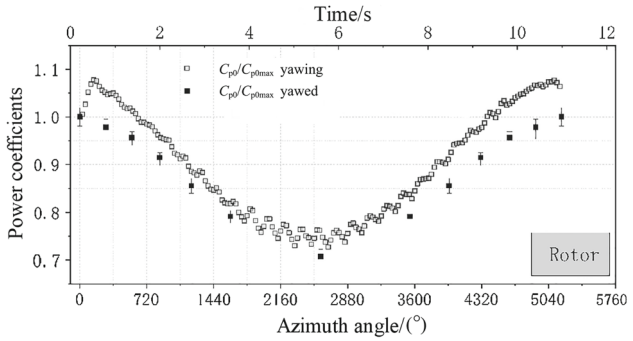

Fig. 27 Comparison of power coefficients of blade between yawed and yawing conditions

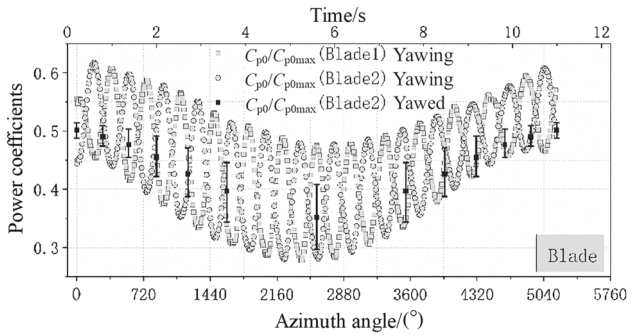

Fig. 28 Comparison of power coefficients of blade between yawed and yawing conditions

Figure 28 shows the variation of power coefficient of the blades between yawed and yawing conditions. It is clearly seen that the power coefficient present larger fluctuation with the variation of yaw angle. The variation law is the same under yawed and yawing condition. At the yaw angle of 30°, the maximum and minimum power coefficients fluctuation of dynamic yawing is 0.48 and 0.27, respectively; while the maximum and minimum power coefficients fluctuation of static yawed is 0.41 and 0.295. The difference is much larger fluctuation of the power coefficients on blade under yawing than that under yawed condition, especially under the non-yawed condition, the variation of the load on blade present much larger than that of yawed case, due to the maximum yaw rate at 0° yaw angle in the process of yawing.

4 Conclusions

Unsteady numerical simulations have been performed in this paper to investigate the unsteady aerodynamic characters of a HAWT under yaw and dynamic yawing conditions. The numerical simulation results show good agreement with measurement data. The aerodynamic characteristics during revolution at different span sections are analyzed in detail. The conclusions can be summarized as follows:

1. Unsteady CFD simulation results give better prediction of aerodynamic performance of HAWT under yaw than BEM method. Transitional SST model has good performance on simulation wind turbine aerodynamics under large yaw angles. The blade load has an obvious fluctuation with the blade passing frequency, and the amplitude increases with the yaw angle. CFD simulation captures the fluctuations with high frequencies due to 3D flow at inner span, which cannot be captured by BEM type methods.
2. The maximum aerodynamic load of the blade moves from the middle span to outer span with the increase of yaw angle. The blade transient loading of 0° azimuth angle nearby is almost monotonically decreased, while in other zone the load increases firstly, then decreases. 3D stall effect presents load fluctuations at the inner board of blade, and becomes stronger with the increasing of yaw angle. Since the variation of angle of attack increases and the value moves towards small value during revolution, the aerodynamic characteristics at all span sections decreases substantially. The averaged powers under yaw angle of 10°, 30° and 60° decrease by 4.265%, 29.9% and 86.8%, respectively. Compared with the result of non-yawed condition, the thrust decrease by 2.32%, 20.37% and 73.98% under yaw angles of 10°, 30° and 60°, respectively, which decreases in cos γ function.
3. The power coefficients under dynamic yawing show much larger power coefficient fluctuations of 0.095 than that of yawed cases, due to the variation of the yaw rate and the additional velocity caused by the dynamic rotation along yaw axis.

The investigation in this paper is performed on a small-scale wind turbine. Further studies have been performed on a large-scale wind turbine. Cross comparisons will be presented in the near future.

Acknowledgements This work was supported by the National Natural Science Foundation of China (Grants 51876063 and 51576065) and the Science and Technology Project of Huaneng Group (Grant HNKJ18-H33) on research and demonstration application of onshore wind energy efficiency improvement technology.

References

1. Micallef, D., Ferreira, C.S., Sant, T., et al.: Experimental and numerical investigation of tip vortex generation and evolution on horizontal axis wind turbines. Wind Energy **19**, 1485–1501 (2016). https://doi.org/10.1002/we.1932
2. Chehouri, A., Younes, R., Ilinca, A., et al.: Review of performance optimization techniques applied to wind turbines. Appl. Energy **142**, 361–388 (2015). https://doi.org/10.1016/j.apenergy.2014.12.043
3. Hand, M. M., Simms, D. A.: Unsteady aerodynamics experiment phase VI: wind tunnel test configurations and available

data campaigns, NREL/TP-500-29955, Technical Report, America, December (2001) https://doi.org/10.2172/15000240
4. Schepers, J.G., Boorsma, K., Cho, T.: Analysis of Mexico wind tunnel measurements: final report of IEA Task 29, Mexnext (Phase 1), Technical Report, ECN-E-12-004, Netherlands, February (2012)
5. Sant, T.: Improving BEM-based aerodynamic models in wind turbine design codes. Ph.D. Thesis, Delft University, Denmark (2007)
6. Micallef, D., Bussel, G.V., Ferreira, C.S., et al.: An investigation of radial velocities for a horizontal axis wind turbine in axial and yawed flows. Wind Energy **16**, 529–544 (2013). https://doi.org/10.1002/we.1503
7. Vey, S., Lang, H.M., Nayeri, C.N., et al.: Utility scale wind turbine yaw from a flow visualization view. In; ASME Turbo Expo 2015: turbine technical conference and exposition, Canada, June 15–19 (2015) https://doi.org/10.1115/gt2015-43407
8. Dai, J., Yang, X., Hu, W., et al.: Effect investigation of yaw on wind turbine performance based on SCADA data. Energy **149**, 684–696 (2018). https://doi.org/10.1016/j.energy.2018.02.059
9. Wang, Y.B., Miao, W.P., Ding, Q.W., et al.: Numerical investigations on control strategies of wake deviation for large wind turbines in an offshore wind farm. Ocean Eng. **173**, 794–801 (2019). https://doi.org/10.1016/j.oceaneng.2019.01.042
10. Ryu, K., Kang, S.H.: Prediction of aerodynamic loads for NREL phase VI wind turbine blade in yawed condition. Int. J. Aeronaut. Space Sci. **17**, 157–166 (2016). https://doi.org/10.5139/IJASS.2016.17.2.157
11. Micallef, D., Sant, T.: A review of wind turbine yaw aerodynamics. In: Wind turbines: design, control and applications, INECH, 27–53 (2016) https://doi.org/10.5772/63445
12. Qiu, Y.X., Wang, X.D., Kang, S., et al.: Predictions of unsteady HAWT aerodynamics in yawing and pitching using the free vortex method. Renew. Energy **70**, 93–106 (2014). https://doi.org/10.1016/j.renene.2014.03.071
13. Peters, D.A., Haquang, N.: Dynamic inflow for practical applications. J. Am. Helicopter Soc. **33**, 64–68 (1988)
14. Gaonkar, G. H., Peters, D.: Review of dynamic inflow modeling for rotorcraft flight dynamics. In: Proceedings of 27th structures, structural dynamics and materials converence, San Antonio, May 19–21 (1988) https://doi.org/10.2514/6.1986-845
15. Suzuki, A.: Application of dynamic inflow theory to wind turbine rotors. Ph.D. Thesis, The University of Utah, USA (2000)
16. Glauert, H.: Airplane propellers. In: Durand, W.F. (ed.) Aerodynamic Theory, pp. 169–360. New York, Springer (1935)
17. Du, Z., Selig, M.A.: 3D stall-delay model for horizontal axis wind turbine performance predictions. In: ASME wind energy symposium, USA, Jan 12–15 (1998) https://doi.org/10.2514/6.1998-21
18. Buhl, M.L.: A new empirical relationship between thrust coefficient and induction factor for the turbulent windmill state. Technical Report, No. NREL/TP-500-36834, National Renewable Energy Laboratory, Golden, CO (2005) https://doi.org/10.2172/15016819
19. Yan, S., Shi, S.P., Chen, X.M., et al.: Numerical simulations of flow interactions between steep hill terrain and large scale wind turbine. Energy **151**, 740–747 (2018). https://doi.org/10.1016/j.energy.2017.12.075
20. Tongchitpakdee, C., Benjanirat, S., Sankar, L.: Numerical simulation of the aerodynamics of horizontal axis wind turbines under yawed flow conditions. J. Sol. Energy Eng. **127**, 464–474 (2005). https://doi.org/10.1115/1.2035705
21. Yu, D.O., You, J.Y., Kwon, O.J.: Numerical investigation of unsteady aerodynamics of a Horizontal-axis wind turbine under yawed flow conditions. Wind Energy **16**, 711–727 (2013). https://doi.org/10.1115/1.2035705
22. Schulz, C., Letzgus, P., Lutz, T., et al.: CFD study on the impact of yawed inflow on loads, power and near wake of a generic wind turbine. Wind Energy **20**, 253–268 (2017). https://doi.org/10.1002/we.2004
23. Jeong, M.S., Kim, S.W., Lee, I., et al.: The impact of yaw error on aeroelastic characteristics of a horizontal axis wind turbine blade. Renew. Energy **60**, 256–268 (2013). https://doi.org/10.1016/j.renene.2013.05.014
24. Dai, L., Zhou, Q., Zhang, Y.W., et al.: Analysis of wind turbine blades aeroelastic performance under yaw conditions. J. Wind Eng. Ind. Aerodyn. **171**, 273–287 (2017). https://doi.org/10.1016/j.jweia.2017.09.011
25. Leble, V., Barakos, G.: 10-MW wind turbine performance under pitching and yawing motion. J. Sol. Energy Eng. **139**, 041003 (2017). https://doi.org/10.1115/1.4036497
26. Wen, B.R., Tian, X.L., Dong, X.J., et al.: A numerical study on the angle of attack to the blade of a horizontal-axis offshore floating wind turbine under static and dynamic yawed conditions. Energy **168**, 1138–1156 (2019). https://doi.org/10.1016/j.energy.2018.11.082
27. Wang, X.D., Ye, Z.L., Kang, S., et al.: Investigations on the unsteady aerodynamic characteristics of a horizontal-axis wind turbine during dynamic yaw processes. Energies **12**, 3124 (2019). https://doi.org/10.3390/en12163124
28. Tian, W., Ozbay, A., Wang, X.D.: Experimental investigation on the wake interference among wind turbines sited in atmospheric boundary layer winds. Acta. Mech. Sin. **33**, 1–12 (2017). https://doi.org/10.1007/s10409-017-0684-5
29. Shirakashi, M., Ueno, S., Ishida, Y., et al.: Vortex excited oscillation of a circular cylinder. Trans. Jpn. Soc. Mech. Eng. **49**, 2102–2110 (1983). https://doi.org/10.1299/jsme1958.27.1120
30. Wang, X.D., Liu, Y.N., Wang, L.Y., et al.: Numerical study of nacelle wind speed characteristics of a horizontal axis wind turbine under time-varying flow. Energies **12**, 3993 (2019). https://doi.org/10.3390/en12203993
31. Somers, D. M.: Design and experimental results for the S809 airfoil. Technique Report, No. NREL/SR-440-6918, Fort Collins, CO, USA: National Renewable Energy Laboratory, January (1997) https://doi.org/10.2172/437668